Thermodynamic stability and diffusion mechanism of LiMXCl$_4$ superionic conductors

KyuJung Jun[1,2,†], Grace Wei[1,2,†], Gerbrand Ceder[1,2,*]

1. Department of Materials Science and Engineering, University of California Berkeley, Berkeley, CA 94720, USA

2. Materials Science Division, Lawrence Berkeley National Laboratory, Berkeley, CA 94720, USA

† These authors contributed equally.

Abstract:

LiMXCl$_4$ is a recently discovered lithium superionic conductor reported with a Li conductivity up to 12.4 mS/cm at room temperature. In this work, we explore various types of M-cation and X-anion substitutions in the LiMXCl$_4$ system. We find that fluoro-chlorides may provide promising thermodynamic and electrochemical stability without compromising ionic conductivity. Ab-initio molecular dynamics simulations on seven substitutions and three lithium concentrations for each substitution suggest that even higher conductivity may be achieved in LiMXCl$_4$ than has been reported. A Meyer-Neldel analysis comparing LiMXCl$_4$, close-packed halides, and LaCl$_3$-type systems demonstrates the potential of the LiMXCl$_4$ family due to their high Meyer-Neldel energy, high prefactor, and low activation energy, projecting a range of conductivity of 10-100 mS/cm. An analysis of the correlation between lithium-ion hops and small-angle tilting events finds that LiMXCl$_4$ systems exhibit a strong cradle effect where weakly bound M-octahedra often tilt their orientation in conjunction with a nearby Li-ion hop to flatten the lithium-ion energy landscape. Such an advantage originates from the fact that in the LiMXCl$_4$ structure, one-dimensional M-octahedral chains are bound via weak van der Waals interactions which can accommodate for reduction in free volume via rotational correlation of the octahedra. Our work demonstrates an exciting direction towards further improving this class of materials in terms of ionic conductivity and electrochemical stability and provides a fundamental understanding of the factors that lead to high ionic conductivity in non-close-packed oxyhalide systems.

1. Introduction

The global transition to renewable energy and the increasing energy demands on the electric grid necessitate the development of novel batteries with improved performance and safety. All solid-state batteries are a promising technology as they use inorganic solid electrolytes (SEs), which are safer compared to their flammable, liquid counterparts. In addition, when coupled with lithium metal anodes, the energy density can be significantly improved compared to current lithium-ion batteries[1].

An ideal solid electrolyte should demonstrate high ionic conductivity and stability across the wide range of lithium chemical potential that lithium ions experience in a full cell. However, previous theoretical and experimental studies have shown that no solid electrolyte material exhibits this criteria[2]. An alternative to this "ideal solid electrolyte" is to utilize two solid electrolyte materials: one with excellent cathodic stability at low voltage (SE_{anode}) and another stable at high voltage ($SE_{cathode}$ or catholyte)[3]. If these two materials are chemically compatible and have overlapping stability windows, this configuration can offer improved stability compared to full cells employing a single solid electrolyte. For example, Zhou and Nazar demonstrated in 2022 that over 1000 cycles can be achieved when using a halospinel-type chloride solid electrolyte as the catholyte and an argyrodite solid electrolyte as the separator against a Li/In anode[3].

For catholytes, high oxidative stability above 4 V is required. One candidate class of materials are the polyanion-based oxide materials such as NASICON-type $Li_{1+x}Al_xTi_{2-x}(PO_4)_3$ or $LiTa_2PO_8$. However, processing these oxides in a cathode composite is challenging. Their

inability to deform plastically necessitates co-sintering with cathode active materials (CAM) to achieve good contact[4,5], often resulting in the degradation of CAM particles and the decomposition of the solid electrolyte material.

As a possible alternative, close-packed chloride SEs have attracted significant attention due to their relatively high ionic conductivity (> 1 mS/cm), excellent oxidative stability, and mechanical softness, which facilitates the fabrication of a cathode composites[6–9]. Prior to 2023, no known halide materials achieved the ionic conductivities observed in state-of-the-art sulfide SEs (10 - 30 mS/cm)[10–12]. This shortfall can be attributed to the close-packed anion arrangement of existing halide conductors, which provides highly symmetric lithium-ion sites that trap lithium ions and confines them to narrow, high-energy *oct-tet-oct* diffusion channels[13].

In 2023, Tanaka *et al*. reported a new Li oxyhalide superionic conductor, $LiMOCl_4$ (M = Nb/Ta), with high ionic conductivities of up to 12.4 mS/cm[14]. Unlike most previously studied chloride-based superionic conductors, $LiMOCl_4$ features a non-close-packed anion framework. The authors proposed that diffusion in $LiMOCl_4$ occurs via a liquid-like conduction mechanism, allowing ions to move uncorrelated with one another. Recently, Singh *et al.* investigated the $LiNbOCl_4$ system using X-ray and neutron diffraction, pair diffraction analysis, and molecular dynamics simulations. They identified the flexible nature of the bonding between Nb-octahedra as advantageous for lithium-ion diffusion[15].

In this work, we perform first-principles calculations and ab-initio molecular dynamics (AIMD) simulations to investigate the thermodynamic and electrochemical stability, as well as the

3

lithium-ion diffusivity and conductivity, of the LiMXCl$_4$ family of superionic conductors (where M = Ta, Nb, Sb, Ti, Zr, Hf, Sn, and X = O, F, Cl) in stoichiometric, lithium-deficient, and lithium-excess compositions. Our findings indicate that all LiMXCl$_4$ systems exhibit superionic conductivity at room temperature and without requiring an excess or deficiency of lithium to activate their high conductivity. Meyer-Neldel analysis of the ionic conductivities in this family reveals that its high Meyer-Neldel energy provides access to an order-of-magnitude higher ionic conductivity compared to close-packed halides or LaCl$_3$-derived systems. By investigating the correlation between the small-angle tilting motion of M-octahedra and lithium-ion hops in molecular dynamics trajectories, we find that the van der Waals bonded framework provides wide channels with weak Li-cation interactions, facilitating good lithium transport. Additionally, this crystal structure maintains high ionic conductivity upon channel shrinkage by activating a soft-cradle effect that lowers the energy as Li migrates from site to site. Our findings provide the theoretical foundation for the effectiveness of the LiMXCl$_4$ family as promising catholytes compatible with 4-V-class cathodes, achieving ionic conductivities of 10-100 mS/cm at room temperature.

4

2. Results

2.1 Crystal structure of oxychlorides with 1-dimensional van der Waals bonds

The crystal structure of $LiMOCl_4$ is illustrated in Figure 1. $LiMOCl_4$ consists of one-dimensional chains of corner-O-sharing MO_2Cl_4 octahedra, with Li occupying tetrahedral sites neighboring the Cl^-. These chains are connected via van der Waals bonding along the *b*- and *c*-directions, with mobile lithium ions occupying the void space between the chains.

Using an approach similar to previously developed compound discovery methods[16], Tanaka *et al.* discovered $LiMOCl_4$ (M = Nb, Ta) by performing double-substitution on $LiVOF_4$ ($V^{5+} \rightarrow Nb^{5+}$ or Ta^{5+} and $O^{2-} \rightarrow Cl^-$) from the Materials Project database[14,17]. $LiVOF_4$ is a hypothetical compound in the orthorhombic *Cmc2₁* space group that has yet to be synthesized (Materials Project ID: mp-850188). Initial structure refinement by Tanaka et al mapped $LiMOCl_4$ (M = Nb, Ta) to the same *Cmc2₁* space group as $LiVOF_4$, suggesting that the two perpendicular directions (b, c-direction in Figure 1) are not equivalent. However, a subsequent study by Adams[18] proposed an alternative structure model for $LiNbOCl_4$ in the tetragonal *I4/m* space group. This model was based on the notion that the two perpendicular directions to the $[NbCl_4O_{2/2}^-]\infty$ chain may be equivalent, with disordered lithium occupancy between the chains. Adams' structure refinement based on the *I4/m* model resulted in a smaller, more symmetric unit cell with an improved weighted profile R-factor (R_{wp}).

Recently, Singh and Wang et al. proposed a lower symmetry model for LiNbOCl$_4$ in the *Cc* space group, where Nb is off-centered within the NbO$_2$Cl$_4$ octahedra, resulting in unequal Nb-O bond lengths along the *a*-direction[15]. To assess whether this lower symmetry structure is applicable to the entire LiMXCl$_4$ (M = Ta, Nb, Sb, Ti, Zr, Hf, Sn, and X = O, F, Cl) family, we performed density functional theory (DFT) relaxations for all our systems with various cation and anion substitutions following the structure model proposed by Tanaka *et al* (denoted as "non-shifted"). To explore the energetic preference of the off-centered M-cation position, we also performed relaxations after artificially shifting the initial M-cation position of Tanaka *et al.*'s model by 0.03 in fractional coordinates along the *a*-direction (denoted as "shifted") to help the cation escape local energy minima. Supporting Information Table A-1 shows the energy differences in eV/atom between the shifted and unshifted structures for all substitutions considered. Our results indicate that, all our systems with cation and anion substitutions, M-cations are more stable in the unshifted structure or relax back to the unshifted position. The only exception is Nb in LiNbOCl$_4$, where the shifted structure is more stable by 11.5 meV/atom. Therefore, the lower symmetry structure is likely applicable only to LiNbOCl$_4$, possibly due to a second-order Jahn-Teller effect as suggested by other work[19,20].

a top view

MO$_2$Cl$_4$ octahedra

Li

van der Waals bonding

b side view
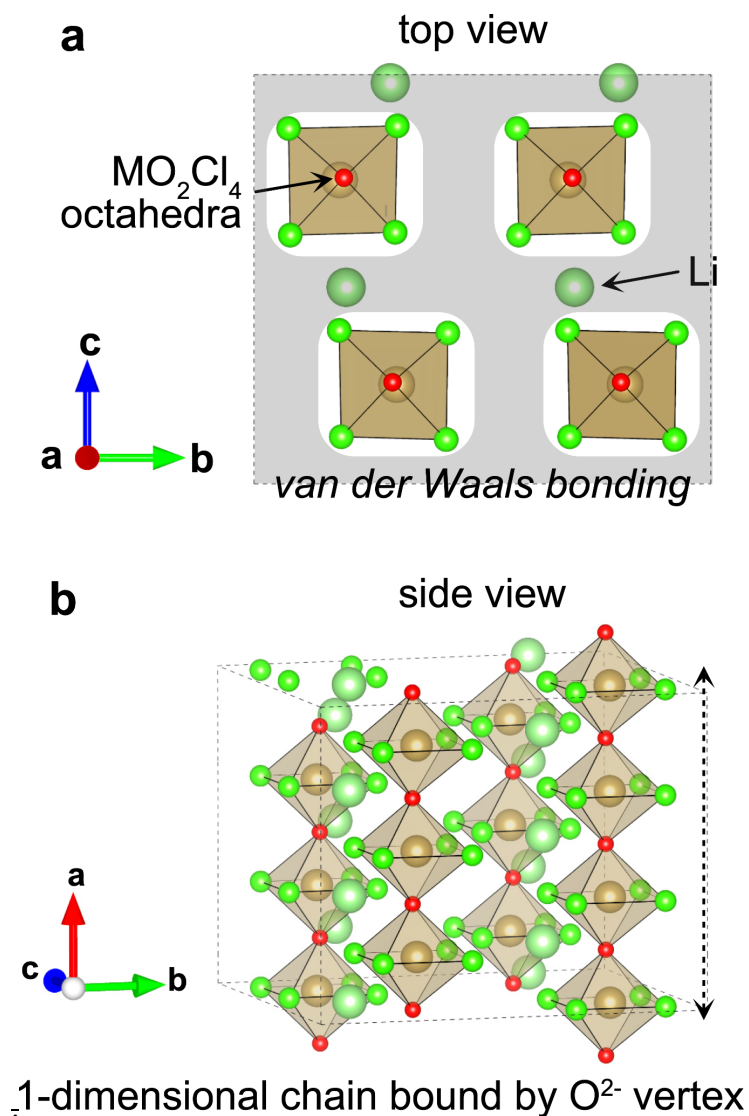
1-dimensional chain bound by O^{2-} vertex

Figure 1. Crystal structure of LiMXCl₄. The crystal structure of LiTaOCl₄ seen from the *a*-direction is shown in (a). View perpendicular to the *a*-direction is shown in (b), showing the 1-dimensional chains of MO₂Cl₄ octahedra. Large green spheres and brown spheres indicate Li and Ta cations respectively. Small green spheres and red spheres indicate Cl and O anions respectively. Grey shaded area in (a) indicates the van der Waals bonding in the *b*- and *c*-direction.

2.2 Chemical substitutions and stability

To explore the possibility of chemical substitutions within the oxychloride structural framework, we analyzed the $LiMXCl_4$ family of superionic conductors. In this family, M can either be a 5+ transition metal (Ta, Nb, Sb) with X = O, or a 4+ transition metal (Ti, Zr, Hf, Sn) with X = F or Cl. We did not consider Br or I substitutions due to their poor oxidative stability[2,21], which would limit their use as catholytes. The compounds $LiTaOCl_4$, $LiNbOCl_4$, $LiSbOCl_4$, $LiTiFCl_4$, $LiZrFCl_4$, $LiSnFCl_4$, and $LiHfFCl_4$ are denoted as LTOC, LNOC, LSOC, LTFC, LZFC, LSFC, and LHFC, respectively.

The phase stability of all $LiMXCl_4$ systems was determined by computing the energy above the convex hull, E_{hull}, using the lowest-energy DFT-relaxed structure from Section 2.1, as presented in Figure 2a. Calculations were performed in the GGA approximation, with more details provided in the Methods section. The tabulated data, including each system's decomposition products, are reported in Supporting Information, Table B-1. The E_{hull} values for the experimentally-observed structures LTOC and LNOC are 7.8 and 13.9 meV/atom, respectively, indicating that these energies are sufficiently low enough for the structures to be synthesizable using a ball milling approach[14,15]. Considering a conservative synthesizability limit of 30 meV/atom[22,23], two additional $LiMXCl_4$ compounds exhibit good potential for synthesis: $LiHfFCl_4$ (with E_{hull} = 10.6 meV/atom, metastable) and $LiZrFCl_4$ (with E_{hull} = 29.1 meV/atom, metastable).

In general, we observe that phase stability in $LiMXCl_4$ systems is impacted by both cation (M) and anion (X) substitutions. For instance, all pure chloride structures are highly unstable, with

$E_{hull} > 60$ meV/atom. F-substituted structures exhibit a broader range of stability, depending on the 4+ cation. The ordering of stable to least stable F-substituted structures by cation is: Hf > Zr > Sn > Ti. Cation substitution in the X = O system also affects the thermodynamic stability, with the stability ranking for O-substituted structures by cation being: Ta > Nb > Sb. The absence of a metastable pure chloride system within this structural framework suggests that a mixed anion framework may be necessary to stabilize the polyhedral chains in the structure. Given that the electronegativity of O and F is higher than that of Cl, it is plausible that the presence of a more electron-withdrawing anion at the octahedron apex connecting the chain is required for stability.

2.3 Electrochemical stability

Electrochemical stability windows were computed for each $LiMXCl_4$ system using the approaches of Richards *et al.* and Zhu *et al.*[24,25], and their oxidative and reductive limits (versus Li metal) alongside their predicted decomposition products are presented in Figure 2b. The tabulated data comprising reduction and oxidation limits is reported in SI Tables B-1 and B-2. For the experimental structures, LTOC is calculated to be thermodynamically stable up to 4.18 V and LNOC up to 4.14 V, making them both compatible with 4 V layered oxide cathodes. However, both systems display poor reductive stability, rendering them incompatible with Li metal. The predicted reaction products for LTOC decomposition against Li metal include LiCl, Ta_2Cl_5, and Ta_2O_5 for LTOC, all of which are electrical insulators that may form a passivating layer. In contrast, the decomposition of LNOC is predicted to produce LiCl and $NbCl_2O$, with $NbCl_2O$ being electrically conductive and potentially leading to the growth of the interface over time. Furthermore, none of the equilibrium decomposition components are likely to be good

9

ionic conductors. Therefore, while these materials exhibit high oxidative stability, their poor reductive stability and unfavorable phase equilibria limit their application as catholytes.

The reductive stability of conductors is typically determined by the lowest reduction potential of the metals present[2,24], while the oxidative stability is controlled by the oxidation of its anion. The latter is influenced by its hybridization with the metals[2,26,27]. In line with these expectations, we observe an increase in oxidative stability for the $LiMFCl_4$ and $LiMCl_5$ systems, with the $LiSnFCl_4$ system exhibiting the highest oxidative stability at 4.47 V. The reductive stability is also improved for M = Zr and Hf systems, with $LiHfFCl_4$ showing a lower stability limit of 1.46 V. This improvement is likely due to the stability of the 4+ oxidation state in Zr and Hf, whereas the other cations (Ta, Nb, Sb, Sn, Ti) tend to reduce to a lower valence state. The Sn^{4+} and Sb^{5+} systems, in particular, demonstrate very poor reductive stability due to their reduction to Sn^{2+} and Sb^{3+}, respectively. Despite the increased stability window for $LiHfFCl_4$ and $LiZrFCl_4$ (2.90 V and 2.53 V) which is wider than for LTOC and LNOC (1.99 V and 1.57 V), the $LiHfFCl_4$ and $LiZrFCl_4$ systems are still not stable against Li metal. Additionally, their decomposition products upon reduction (HfF_4, Hf, $ZrCl_3$, Li_2ZrCl_6, Li_2HfCl_6, $Li_3Zr_4F_{19}$) include metallic elements (e.g., Hf) and/or products unstable against Li metal (e.g., Li_2ZrCl_6 and Li_2HfCl_6). Thus, although these limitations would still confine them to being catholytes, their improved oxidative and reductive stability could result in better compatibility with higher voltage cathodes and lower voltage anolytes. In general, all $LiMXCl_4$ systems may serve as catholytes due to their oxidative stability exceeding 4V. However, their poor reductive stability necessitates a separate anode-side solid electrolyte (such as Li_3YCl_6 used by Tanaka *et al.*) to bridge the lithium chemical potential down to the anode for functioning in all-solid-state batteries.
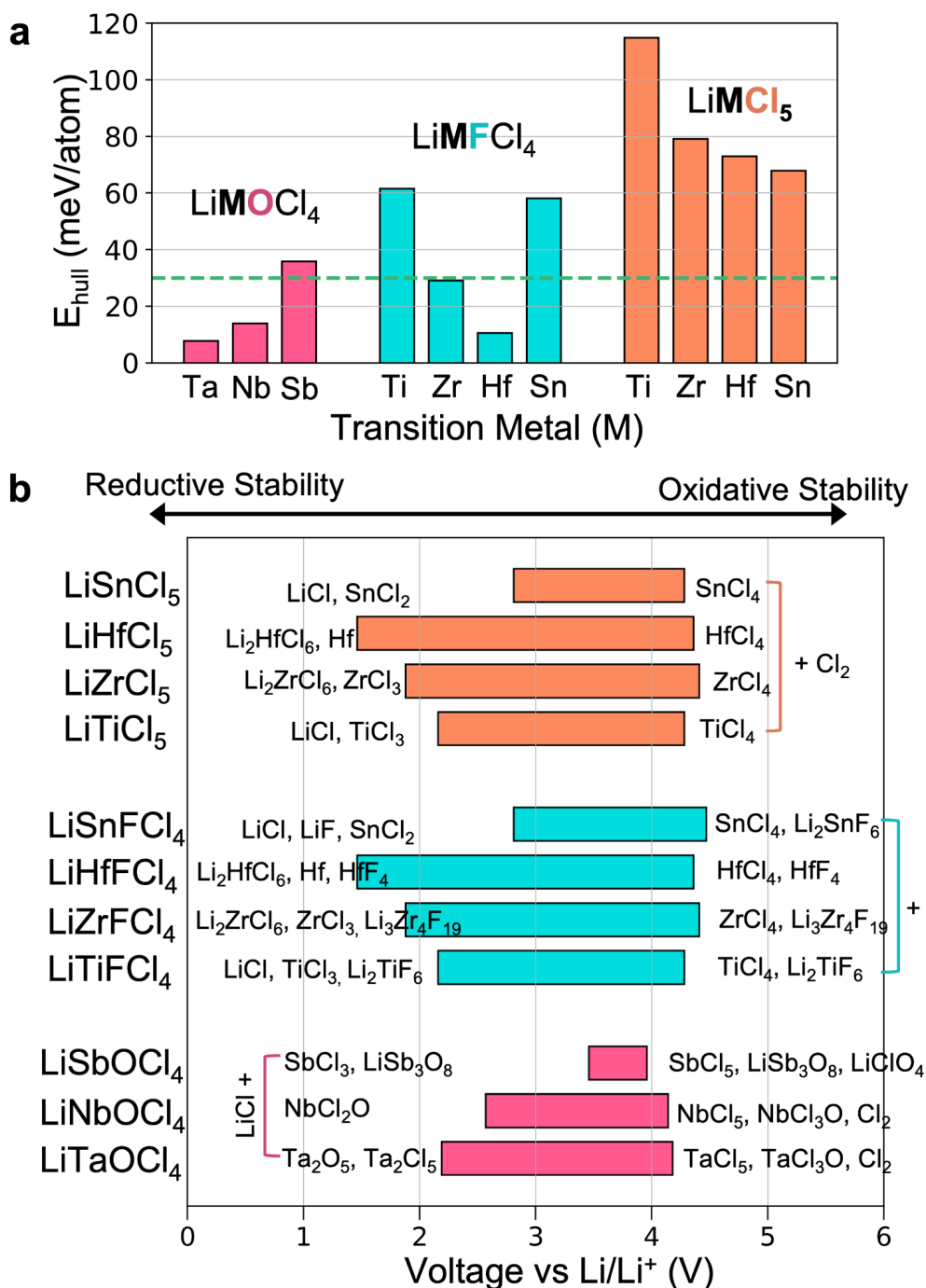
11

Figure 2. Thermodynamic and electrochemical stability of LiMXCl₄ (M = Ta, Nb, Sb, Ti, Zr, Hf, Sn, X = O, F, Cl). (a) The energy above the convex hull E_{hull} computed for LiMXCl₄ systems in the GGA approximation. The horizontal green dashed line at E_{hull} = 30 meV/atom denotes a conservative limit of metastability, where systems with E_{hull} < 30 meV/atom may be

synthesizable. **(b)** Electrochemical stability windows computed for LiMXCl$_4$ systems using the approach in Richards et al. and others[2,24,25]. The voltage is taken w.r.t. Li/Li$^+$. The decomposition products at the reductive and oxidative limits are listed next to the respective stability window. Colors for (a) and (b) correspond to the type of substitution performed (orange = M$^{5+}\rightarrow$ M^{4+} and X→Cl substitution, cyan = M$^{5+}\rightarrow$ M^{4+} and X→F substitution, pink = M$^{5+}\rightarrow$ M^{5+} substitution).

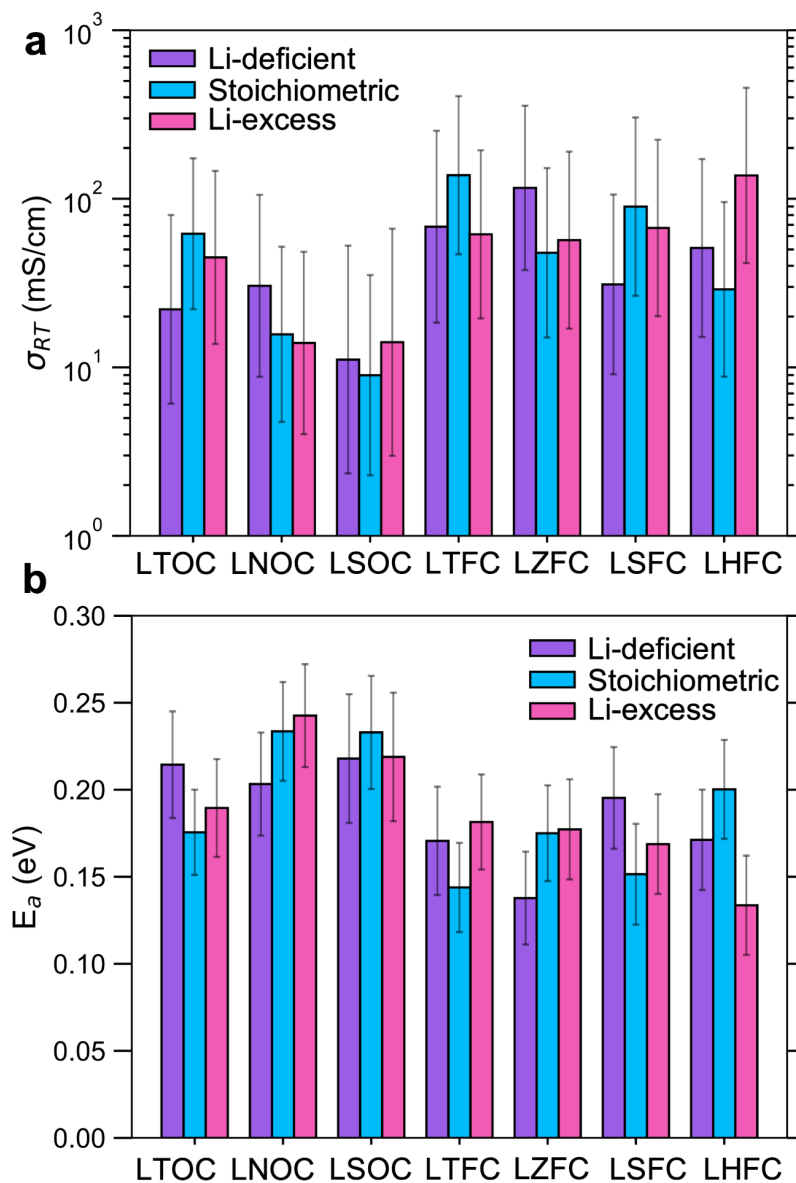# 2.4 Li$^+$ Diffusivity and Conductivity

Figure 3. Room-temperature (a) calculated ionic conductivity and (b) activation energy of LiMXCl$_4$ (M = Ta, Nb, Sb, Ti, Zr, Hf, Sn, X = O, F) for stoichiometric, Li-deficient, and Li-excess compositions. Values are extrapolated from AIMD simulations for 0.4 ns at 5 temperatures between 600-800 K.

14

To evaluate the Li transport in the $LiMXCl_4$ family, we conducted AIMD simulations on oxy- and fluoro-chloride systems at 600, 650, 700, 750, and 800K. Pure chloride systems ($LiMCl_5$) were excluded due to their high decomposition energies (Fig. 2a). All AIMD simulations were run for at least 0.4 ns at each temperature. To account for the effect of Li off-stoichiometry, which has often shown to be beneficial to Li conduction in inorganic conductors[28,29], we also considered Li-excess and Li-deficient compositions for the $LiMXCl_4$ systems. This was achieved by adding one lithium ion to the lowest energy position or removing one lithium ion from the highest energy position in a 60-anion supercell while applying a background charge for charge compensation (see Methods for details). Thus, a total of 42 ns AIMD simulations were conducted for this work. The AIMD simulations were initialized from the structure reported by Tanaka *et al.*, which does not account for the possible lowering of energy via off-centering of the M-cations. We anticipate this to have little effect on the results, as we observe a bimodal distribution of Nb-O bond distance in AIMD simulations which indicates a spontaneous off-centering of Nb. Notably, among all investigated systems, only $LiNbOCl_4$ exhibits off-centering of the M-cation in AIMD simulations, which is consistent with our observations in the DFT relaxations discussed in Section 2.1. Further discussion on this matter is provided in SI Figure C-1.

Figure 3 shows the extrapolated room-temperature lithium ion conductivities (Fig. 3a) and activation energies (Fig. 3b) for the seven oxy- and fluoro-chloride systems. The Arrhenius plots for each system are presented in SI Figure D-1. Our extrapolated results display good agreement with experimental data for the known conductors. The extrapolated room-temperature

conductivity of LNOC in our calculations is 15.7 [4.7, 51.9] mS/cm, closely aligning with the experimental value reported by Tanaka et al. of 10.7 mS/cm. Additionally, our computed activation energy of 0.23 ± 0.03 eV is very close to the experimental value of 0.24 eV. For LTOC, our extrapolated results do not align with experimental data as well as they do for LNOC. We computed an activation energy of 0.18 ± 0.03 eV compared to the experimentally reported value of 0.23 eV, and an extrapolated room-temperature ionic conductivity of 62 [22.1, 173.6] mS/cm compared to the experimentally reported value of 12.4 mS/cm. However, our results show the same qualitative trend as the experimental results, with LTOC achieving higher ionic conductivity than LNOC. Additionally, all Arrhenius curves appear well-resolved with little error and are linear across the temperature range simulated (600 - 800 K). Some possible explanations for the discrepancy between our theoretical results and reported experimental results include the assumption of the Nernst Einstein relation, which ignores Li-Li correlations in the computations[30], large error bars due to limited simulation timescales, and possible non-Arrhenius behavior at lower temperatures[18].

All simulated $LiMXCl_4$ structures display conductivity greater than 1 mS/cm at room temperature. Additionally, all systems, except stoichiometric $LiSbOCl_4$, show RT conductivity above 10 mS/cm, the highest among any known halide conductors. The $LiMXCl_4$ family also displays activation energies (0.13-0.24 eV) that are substantially lower than the best activation energies achieved for close-packed halides (~ 0.3 eV)[31,32] and similar to the activation energy observed in the non-close-packed $LaCl_3$-type conductors (0.197 eV)[13,33]. The range of conductivities computed is quite large, from 9 mS/cm for stoichiometric $LiSbOCl_4$ to 137.5 mS/cm for Li-stuffed $LiHfFCl_4$. Some of the large discrepancies may be attributed to simulation

error due to the limited time scales available via AIMD. However, as not all the error bars can be explained as such, it is possible that the ionic conductivity in the $LiMXCl_4$ family can be significantly improved beyond what has been initially reported by Tanaka et al, whether by introducing off-stoichiometry and/or tuning the cation and anion chemistry.

Comparing the extrapolated room-temperature conductivity values for stoichiometric, Li-excess, and Li-deficient materials (Fig. 3a), it is apparent that off-stoichiometry is not necessary for good conductivity in this structural framework. As all stoichiometric structures display RT conductivity greater than 9 mS/cm, it is clear that the stoichiometric phase already exhibits a good balance between occupied and unoccupied Li sites[28], and therefore Li stuffing or the creation of vacancies is not necessary to "activate" the diffusion mechanism in this material. Hence, a major advantage of the $LiMXCl_4$ family is that we do not face the doping challenge associated with creating Li-excess or Li-deficient systems.

Based on the above analysis, we aim to rationalize two key points. First, the wide range conductivity values predicted in the $LiMXCl_4$ family (9 mS/cm to 137.5 mS/cm) prompts an investigation into the factors causing these variations within systems that share the same structural framework. Secondly, despite having activation energies comparable to non-close-packed $LaCl_3$ systems (0.13 - 0.24 eV vs 0.197 eV), the oxy- and fluoro-chlorides in the $LiMXCl_4$ framework exhibit significantly higher room-temperature ionic conductivities (9 - 137.5 mS/cm vs. 3.02 mS/cm). To explore these observations, we conduct an analysis using the Meyer-Neldel framework, which relates activation energy and conductivity prefactor in conductors[34]. The Meyer-Neldel rule has been observed in many common ionic conductors,

including oxides and argyrodites[34–37].

In Fig. 4a, we show a Meyer-Nelder-Conductivity (MNC) plot for the oxy- and fluoro-chlorides, illustrating the relationship between the conductivity prefactor σ_0 and the activation energy E_a. Except for $LiSbOCl_4$ (LSOC, cyan), we observe that $ln\sigma_0$ and E_a exhibit a linear correlation within the $LiMXCl_4$ family, indicating that these conductors obey the Meyer-Neldel rule. The linear fit across the $LiMXCl_4$ systems, disregarding LSOC, is depicted by the black dashed line in Fig. 4a and has a R^2 score of 0.95. The inverse of the slope of the MNC linear fit is also known as the Meyer-Neldel energy Δ_0, and the relative magnitude between Δ_0 and the thermal energy k_BT dictates the relationship between a system's conductivity and its activation energy. If $\Delta_0 > k_BT$, then the system's conductivity can be improved by lowering its activation energy. If $\Delta_0 \approx \mathbf{k}_BT$, then the system's conductivity is independent of its activation energy, and if $\Delta_0 < k_BT$, then the system's conductivity will be decreased by lowering its activation energy. From Fig. 4a, we compute Δ_0 to be 60 meV, which is greater than k_BT (26 meV). This suggests that lowering the activation energy could significantly improve the ionic conductivity in this structure. The broad range of conductivity values observed is likely a direct consequence of the varying activation energies (0.13 - 0.24 eV). In Fig. 4b, we demonstrate the direct correlation between activation energy and conductivity, showing a nearly linear relationship between $log(\sigma_{RT})$ and E_a.

To determine how the $LiMXCl_4$ systems compare against other notable Li-ion conductors, we plot their MNC curve alongside the MNC curves of argyrodites$Li_6PS_5Cl_{(1-x)}Br_x$[38], garnets $Li_6MLa_2Ta_2O$[39], close-packed halides $Li_3Y_{(1-x)}In_xCl_6$[40], and the family of non-close-packed

LaCl$_3$-derived conductors Li$_x$Ta$_y$La$_z$Cl$_3$, y/z=½[33] in Fig. 4c. The background includes dashed gray lines representing reference MNC lines for hypothetical materials obeying the Arrhenius relation at 300K for selected ionic conductivities (0.0001 mS/cm - 1000 mS/cm). Detailed computational methods are provided in the Methods section. All the systems in Fig. 4c show good Meyer-Neldel fits, with their exact values and chemistries detailed in Supporting Information Tables E-1 and E-2. We observe that the non-close-packed halide conductors (our studied LiMXCl$_4$ system and the LaCl$_3$ system) exhibit substantially lower activation energies than the close-packed halide, argyrodite, and oxide systems. This observation supports previous claims that a non-close-packed anion framework is necessary for achieving activation energies below 0.3 eV[13].

Fig. 4c also helps explain why the two non-close-packed chloride systems, the LiMXCl$_4$ system and the LaCl$_3$ system, have significantly different ionic conductivities (9 - 137.5 mS/cm vs. 3.02 mS/cm). The MNC line for the LiMXCl$_4$ systems intersects the 10 mS/cm and 100 mS/cm lines, suggesting that, depending on the specific activation energy, the room-temperature conductivity will range between 10 and 100 mS/cm. The LaCl$_3$ system, on the other hand, has a smaller conductivity prefactor, and therefore only crosses the 1 mS/cm line. In addition, the MNC plot for the LaCl$_3$ system has a steeper slope, resulting in a smaller Meyer-Neldel energy compared to the LiMXCl$_4$ systems (29.4 meV vs 60 meV). Since this Meyer-Neldel energy is close to the thermal energy, the conductivity of the LaCl$_3$ system is practically independent of its activation energy. This suggests a limit to the conductivity of LaCl$_3$ systems, as improving their activation energy will not significantly improve their ionic conductivity, limiting the LaCl$_3$ systems to a conductivity near 1 mS/cm. Similar to the LiMXCl$_4$ system, the ionic conductivity for the close-

packed LYC system also improves as the activation energy decreases. However, the range of activation energies (> 0.33 eV) observed will limit their conductivity to < 10 mS/cm.

The combined MNC plots in Fig. 4c indicate that among the presented ionic conductors, compounds in the $LiMXCl_4$ family show possibly the greatest potential due to their combination of low activation energy, high conductivity prefactor, and high Meyer-Neldel energy, which enables their conductivities to be > 10 mS/cm. Finding ways to further lower the activation energy in these systems would allow for the conductivity to reach even higher values. Therefore, identifying factors that decrease the activation energy in these conductors would certainly be beneficial, albeit not necessary, given their preexisting high conductivity.
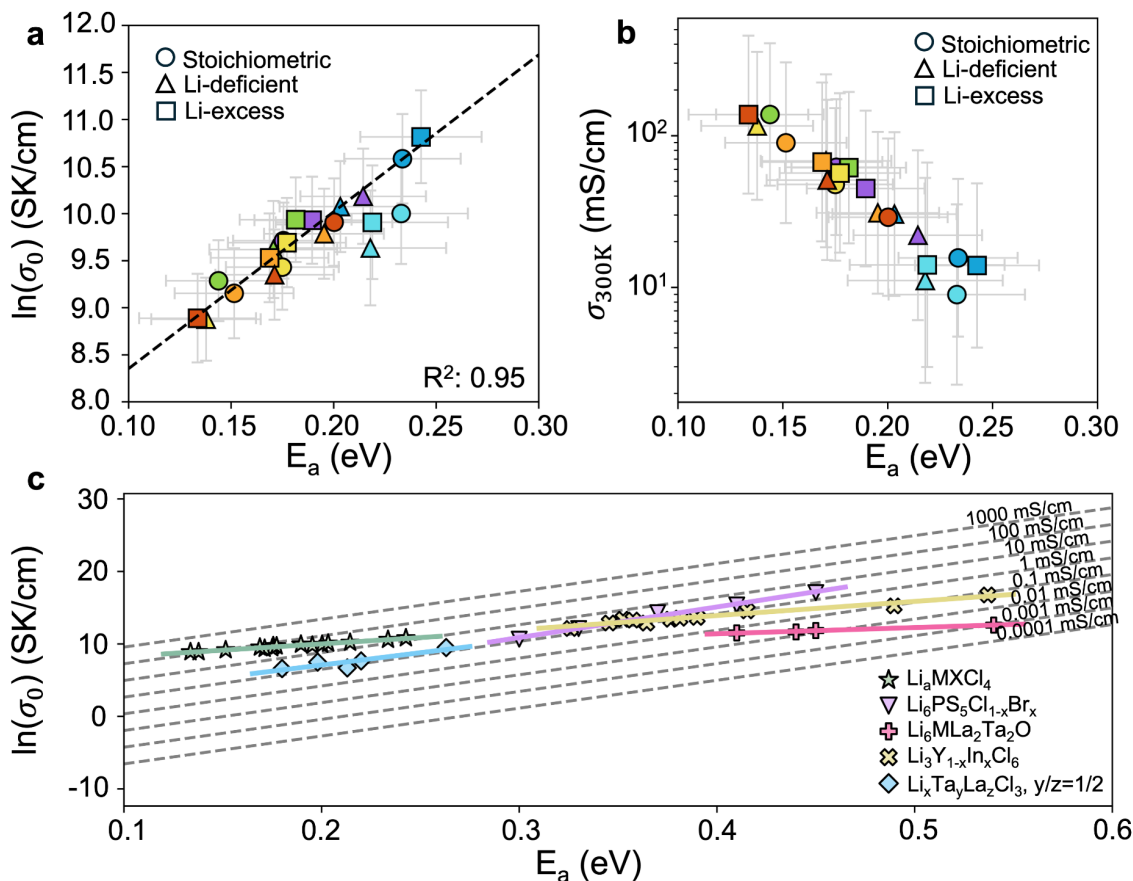
Figure 4. Meyer-Neldel relationship in oxychlorides. (a) Meyer–Neldel–conductivity (MNC) plot for systems in the LiMXCl$_4$ family, plotting the conductivity prefactor against the activation energy. A linear fit on all systems except LSOC is shown by the black dashed line, with a R^2 score of 0.95. (b) Room-temperature conductivity vs. activation energy for all LiMXCl$_4$ systems. For (a) and (b), the colors represent different chemistries: purple = LTOC, blue = LNOC, cyan = LSOC, green = LTFC, yellow = LZFC, orange = LSFC, red = LHFC, and shapes represent different stoichiometries as indicated in the legend. (c) MNC plots for various SSEs as taken from the literature[33,38–40]. The dashed lines correspond to guidelines for different ionic conductivities, as labeled.

2.5 Origin of superionic conductivity in oxyhalides system

Due to the framework cations being connected in a chain via a single vertex (O^{2-} in case of LTOC/LNOC) and the soft van der Waals bonding between the chains, the M-octahedra in $LiMXCl_4$ are capable of tilting their orientation with respect to the chain axis. This tilting may occur independently of lithium-ion hops (as librational motion) or be dependent on lithium-ion hops (i.e. soft-cradle effect)[41]. In this section, we quantify the degree of correlation between Li-ion hops and octahedral tilting and evaluate how octahedral tilting influences the Li-ion conductivities in the $LiMXCl_4$ systems.

Using a previously developed quaternion algorithm for detecting the rotational motions of polyhedra from MD trajectories, we extracted the frequencies of rotational events that exceed various minimum angle cutoffs[41,42]. A similar algorithm was applied to detect the occurrences of individual Li-ion hops with a minimum distance cutoff of 3 Å in MD trajectories (see Methods for details). Figure 5a plots the frequency at which rotation events exceeding a given angle cutoff (15° to 35°) occur for stoichiometric $LiMXCl_4$ at 700 K (data for other temperatures are provided in Supporting Information Figures F-1 to F-5). The horizontal dashed lines indicate the event frequency of lithium-ion hops. In all $LiMXCl_4$ systems, no large-angle rotational motion was detected in our AIMD simulations. Instead, we find a substantial frequency of 20-30° small-angle tilting events comparable to the frequency of lithium hops at all simulated temperatures. For example, the frequency of rotation events exceeding 20° in stoichiometric LTOC at 700 K is 0.483 events/ps/atom, which is comparable to the frequency of lithium-ion hops, 0.496 events/ps/atom. Upon comparing against the rotational motion of Ti-octahedron in the three-

dimensionally covalent bonded NASICON-type $Li_{1.33}Al_{0.33}Ti_{1.67}(PO_4)_3$ (LATP) superionic conductor, we find that while the ionic conductivity of LATP is comparable to those found in $LiMXCl_4$ systems, the frequency of 15°-20° rotational motion is at least an order-of-magnitude smaller. We note that for LATP, rotational motion above an angle of 25° could not be observed in our MD simulations. In general, we observe that the lithium-ion hop frequency in $LiMXCl_4$ systems is similar for all substitutions, whereas the event frequencies of small-angle rotational events vary with chemistry. The order of rotational frequencies is approximately LSFC > LTFC ~ LSOC > LTOC ~ LNOC > LZFC > LHFC.

By performing an Arrhenius fit on the multi-temperature event detection data, we calculated the activation energy of lithium hop events and M-octahedral rotation events. Figure 5b compares the activation energy of 15°, 20°, and 25° rotational events and lithium-ion hop events extracted from the AIMD simulations for stoichiometric $LiMXCl_4$ systems, as well as for LATP at temperatures between 600 K and 800 K (data for Li-excess and Li-deficient systems are provided in Supporting Information Figure G-1). In general, we find that the activation energy of lithium-ion hop events in $LiMXCl_4$ systems is similar to that of 15° rotation events. While the activation energy of Li-ion hops is generally consistent across different chemistries, the activation energy for 20° and 25° rotation events varies significantly by chemistry. The activation energies of rotational events are the lowest for LHFC and LTFC, whereas LSFC, LZFC, and LNOC exhibit the highest activation energy for 20-25° events. When comparing the $LiMXCl_4$ systems with covalently bonded LATP, we find that LATP has noticeably higher activation energies for rotational motion with angles of 15-20°. The activation energy of rotational motions for angles above 25° could not be calculated for LATP because we could not detect sufficient rotational

events above 25°. This result confirms that, in general, the binding of polyhedra within LiMXCl$_4$

structures is much less rigid compared to three-dimensionally covalent frameworks.
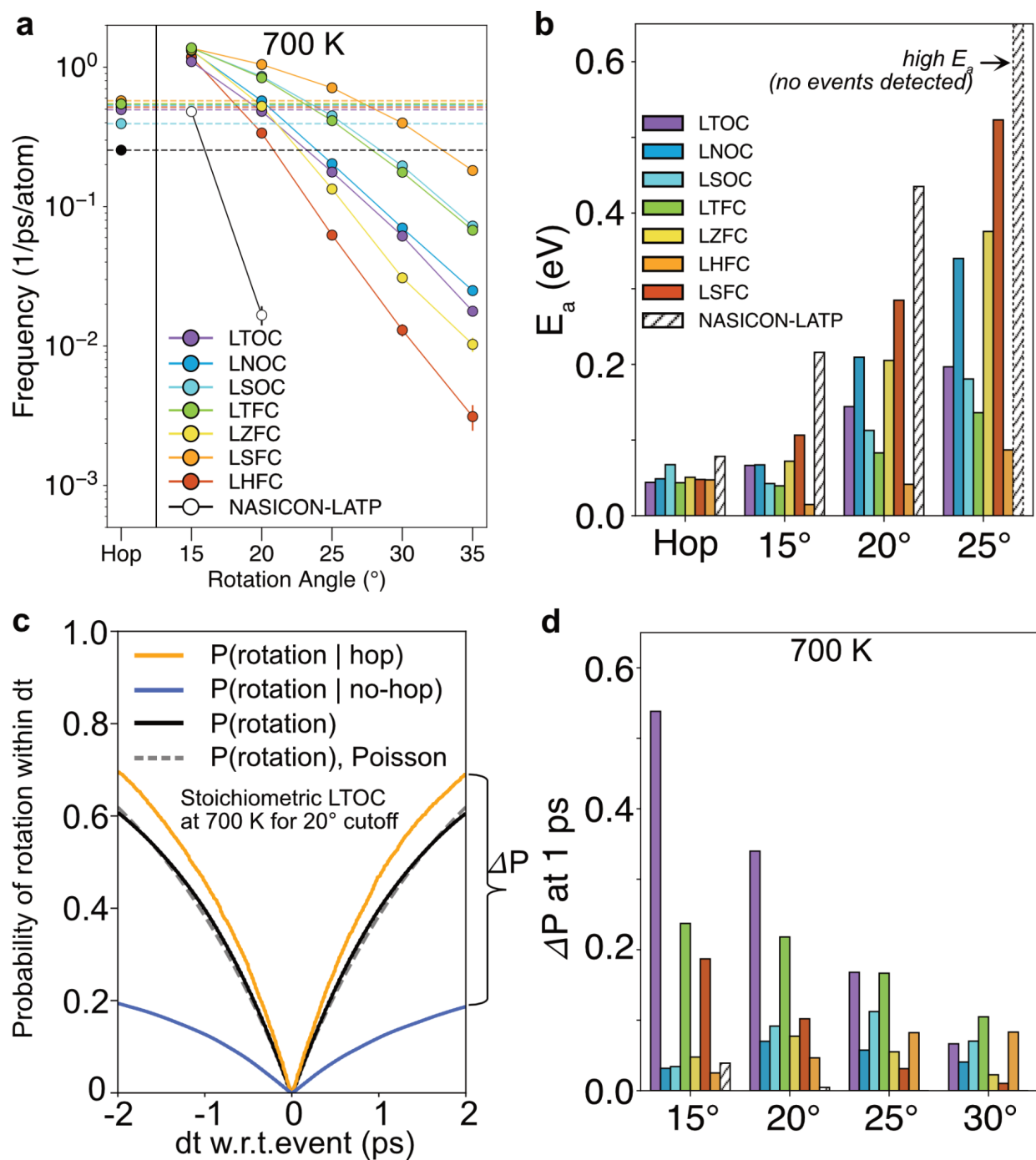

Figure 5. **Relating the rotational motion of octahedra to lithium-ion hops.** The frequency of

Li-ion hop and octahedral rotational motion at 700 K is shown in (a) for stoichiometric $LiMXCl_4$ compounds and for NASICON-type LATP. The dashed horizontal line indicates the frequency of the lithium-ion hops. The activation energy of a Li-hop, and 15°, 20°, and 25° rotation events are plotted for stoichiometric $LiMXCl_4$ and for NASICON-type LATP (b). An arbitrarily high activation energy is plotted for the 25° rotational motion of LATP value as these events were too rare to compute an activation energy. The conditional probability analysis of 20-degree rotations for stoichiometric $LiTaOCl_4$ at 700 K is shown in (c). The orange and blue lines indicate the probability of rotation with the condition that a nearest neighboring Li-ion underwent a hop (orange) or with the condition that the nearest neighboring Li-ion did not undergo a hop within ± 2 ps time window. The black line indicates the probability of a rotation event of a lower-bound angle of 20° occurring regardless of lithium-ion hops. The dashed gray lines indicate the probability of a single octahedral rotation event of a lower-bound angle of 20° occurring within ± dt assuming that rotation events follow a Poisson process. ΔP values at dt = 1 ps for stoichiometric $LiMXCl_4$ and LATP are plotted for 700 K simulations (d).

A similar frequency of 20-30° small-angle tilting events and lithium-ion hop events does not necessarily guarantee that the two motions are spatially and temporally correlated. To understand the degree of correlation between small-angle rotational motion and lithium-ion hops, we calculated the probability of M-octahedra rotational events occurring with the condition that the nearest neighboring Li undergoes a hop within ± 2 ps (P(rotation | hop)) and the probability of M-octahedra rotational events occurring with the condition that the nearest neighboring Li does not undergo a hop within ± 2 ps (P(rotation | no-hop)). As an example, Figure 5c plots these computed conditional probabilities as a function of the time between the hop and rotation event

(dt) in the 700 K MD simulation of stoichiometric LTOC. The orange and blue lines indicate P(rotation | hop) and P(rotation | no-hop), respectively. In stoichiometric LTOC, P(rotation | hop) is significantly higher than P(rotation | no-hop). The gap between the orange and blue lines indicates how much more likely a rotation event is to occur when accompanied by a nearest neighboring Li-ion hop within ± 2 ps. We refer to this difference between P(rotation | hop) and P(rotation | no-hop) as ΔP throughout this work. A positive ΔP indicates that lithium-ion hops are more likely to occur when accompanied by a small angle tilting event of the nearest neighboring M-octahedra, a correlative motion coined the soft-cradle effect[41]. Therefore, since the LTOC system has a significant ΔP (Fig. 5c), it has a prominent soft-cradle effect.

We computed the ΔP values (at dt = ±1 ps) for all stoichiometric $LiMXCl_4$ systems as well as for covalently bonded LATP (Fig. 5d). Figure 5d plots the ΔP values of 15°, 20°, 25°, and 30° rotational events computed from AIMD simulations at 700 K. In all $LiMXCl_4$ systems, ΔP values are positive, indicating that small-angle rotational motions are more likely to occur when accompanied by nearby Li-ion hop. However, the degree of this correlation varies significantly by system. The ΔP values in LTOC and LTFC are significantly larger than in the other $LiMXCl_4$ systems. Hence, while the soft-cradle effect is present in all $LiMXCl_4$ systems, its strength and significance differ by system. Nevertheless, when comparing $LiMXCl_4$ systems against covalently bonded LATP, we find that ΔP values for LATP are near zero at all simulated temperatures (complete data is provided in Supporting Information Figure H-1 to H-5), indicating little correlation between the rotational motion of Ti-octahedra and lithium-ion hops. This analysis suggests that the weakly bound van der Waals framework in $LiMXCl_4$ systems allows the M-octahedra to frequently tilt together with nearby lithium hops, a feature not

observed in covalently bonded systems like LATP.

However, if the correlated rotational motion of the polyhedra were solely responsible for the high conductivity in LiMXCl$_4$ systems, we would expect to observe significant differences in room-temperature conductivities and activation energies between systems with markedly different ΔP values (e.g., LTOC and LZFC). This is not the case, as LZFC, with small ΔP values, and LTOC, with large ΔP values, have very comparable room-temperature conductivities and activation energies. This suggests that a decrease in correlated rotational motion (ΔP) should be offset by a positive factor beneficial to Li diffusion.

In Figure 6a, we plot how ΔP (the degree of correlation between 20° tilting motion and lithium-ion hop) is affected by free volume and the M-octahedra volume for all stoichiometric LiMXCl$_4$ systems at 650 K. The average volume of M-octahedra was computed by sampling the M-octahedral volume every 1 ps from the AIMD snapshots at each temperature. We compute the free volume that a lithium-ion can access by subtracting the average volume of M-octahedra from the supercell volume. We find that the degree of correlation between octahedral tilting and lithium-ion hop is larger when the free volume and the volume of M-octahedra are smaller.

To rationalize this observation, we propose that both the free volume for lithium diffusion and the strength of interaction between lithium-ion and M-cations govern the degree of correlated rotational motion in the LiMXCl$_4$ framework (Fig. 6b-c). If there is sufficient free volume for lithium to diffuse or if the interaction between M-cations and lithium ions is weak, lithium can

27

diffuse through the structure with minimal cation repulsion within the diffusion channel, reducing the need for 20°–30° tilting of M-octahedra to facilitate lithium-ion hops. However, as the free volume for lithium decreases and the interaction between the M-cations and lithium ions strengthens, more octahedral tilting is needed to facilitate lithium-ion hopping. Larger octahedra elongate the distance between the Li ions and M-metal cations, hereby lowering the interaction between them. Consequently, a larger octahedral volume correlates with less correlated octahedral tilting.

Thus, the wide channels and weak interaction from M-cations in $LiMXCl_4$ structures provide fast lithium transport. However, even in $LiMXCl_4$ systems where the channel size may be relatively smaller and the interaction from M-cations is relatively stronger, their flexible van der Waals frameworks can still facilitate fast lithium transport by enabling the soft-cradle effect.
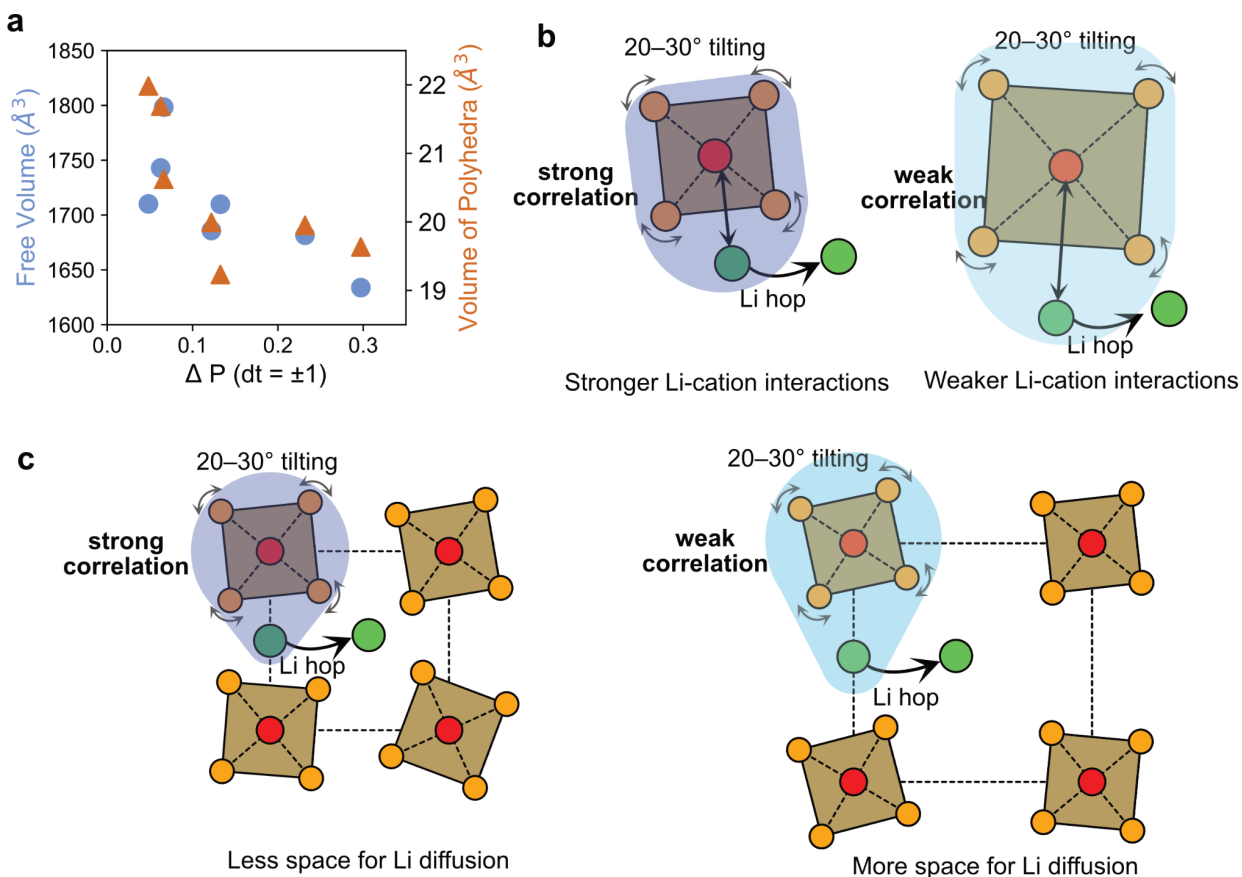
Figure 6. Rationalization of the degree of correlated rotational motion in LiMXCl$_4$ systems. . (a) plots the trend between ΔP (the degree of correlation between 20° tilting motion and lithium-ion hop) and free volume (defined by the supercell volume subtracted by M-octahedra volume, blue) as well as volume of M-octahedra for all stoichiometric LiMXCl$_4$ systems at 650 K (brown). **(b)** Schematic showing how a smaller M-octahedra volume results in stronger interaction to a nearby lithium resulting in a stronger degree of correlation between its 20° rotational motion and a nearby lithium-ion hop. **(c)** Schematic where a smaller free volume in the crystal structure provides less space for lithium diffusion, resulting in a stronger correlation between its 20° rotational motion and a nearby lithium-ion hop.

29

3. Discussion

The recently discovered oxychloride structure shows immense potential as a solid-state catholyte due to its high oxidative stability, ionic conductivity, and soft mechanical response compared to pure oxides. Additionally, oxychlorides have the advantage that their high conductivities do not deteriorate upon heat treatment[14,15]. This differs from close-packed halides, where defects such as stacking faults or cation disorder are typically required for superionic conductivity, causing close-packed halides to lose their superionic conductivity at temperatures as low as $60°C$[31,43]. Our results show that the high ionic conductivity and oxidative stability are not limited to the reported $LiNbOCl_4$ or $LiTaOCl_4$ but can also be achieved in other cation- and anion-substituted systems. This suggests potential for further improvements in ionic conductivity and the development of more cost-effective alternatives to Nb- or Ta-systems, such as those based on Ti, Sn, and Zr.

Our first-principles calculations also suggest that the oxychloride structure may be realized with a fluoro-chloride chemistry. In particular, the concurrent substitution of high-valent cations Ta^{5+} and Nb^{5+} with lower valence cations Zr^{4+} and Hf^{4+}, and O^{2-} with F^-, may improve the reductive stability while maintaining reasonable thermodynamic stability. We find that pure chlorides are highly unstable in this framework, indicating that a mixed anion framework with a distinct anion (O or F) connecting the octahedra may be key to stabilizing the structure. Although many of the $LiMXCl_4$ compounds are computed to be metastable, none are thermodynamically stable at zero K, likely explaining why ball-milling has been the primary method of synthesis for these materials.

Another advantage of the LiMXCl$_4$ compounds is that no additional Li off-stoichiometry substitutions are required to achieve high ionic conductivity, unlike in garnets or NASICON-type conductors. In garnets, introducing excess lithium beyond a lithium content of 3 is necessary to achieve room temperature superionic conductivity[44]. Similarly, NASICON-type LiTi$_2$(PO$_4$)$_3$ requires excess lithium content above 1.3 to achieve high conductivity[45,46]. In contrast, the LiMXCl$_4$ family exhibits superionic conductivity across stoichiometric, lithium-deficient, and lithium-excess compositions, without a systematic trend between lithium off-stoichiometry and ionic conductivity. This indicates that LiMXCl$_4$ materials do not require the strong lithium-lithium interactions induced by Li stuffing to achieve a flat energy landscape.

Instead, a number of fundamental factors contribute to generating higher ionic conductivity in LiMXCl$_4$ compared to any previously reported close-packed chloride conductors, which at best achieve ionic conductivities of approximately 3 mS/cm at RT. Firstly, the LiMXCl$_4$ structure is built from a non-close-packed framework with corner-sharing connectivity between the M-octahedra. It was previously suggested that corner-sharing oxide frameworks facilitate fast lithium-ion diffusion by providing highly distorted Li-sites[29]. The distortion of Li sites away from perfectly symmetric tetrahedral or octahedral configurations lowers the kinetically resolved activation energies needed to escape each coordination environment. This is a major cause for the lower activation energy and improved room-temperature conductivity in the LiMXCl$_4$ structure compared to close-packed chlorides, as supported by recent studies[13]. Another advantage of corner-sharing frameworks is the low spatial density of non-Li cations, which increases the likelihood of lithium ions migrating without approaching the positive charges of the non-Li cations. LiMXCl$_4$ compounds benefit from this feature, having a non-Li cation to anion

ration of 1:5, which is lower than all oxide-based superionic conductors (NASICON: 5:12, garnet: 5:12, $LiTa_2PO_8$: 3:8). We believe this factor may also be advantageous for close-packed chlorides (Li_xMCl_6: 1:6) and may be the reason why amongst the diverse M:Cl ratios possible in close-packed halides, only the smallest M:Cl ratio of 1:6 results in superionic conductivity (e.g., Li_3MCl_6 (M = Y, In, Er), Li_2ZrCl_6).

Another characteristic feature that benefits lithium-ion diffusion in the $LiMXCl_4$ system is its van der Waals bonded framework. The M-octahedra are connected to each other by a single O^{2-}/F^-/Cl^- vertex, forming one-dimensional M-octahedral chains. These chains interact with one another only via van der Waals interactions, allowing for a flexible framework response towards migrating lithium ions, helping to flatten the lithium-ion energy landscape. This concept is supported by our comparison of the degree of correlation between 20° octahedral rotations and lithium-ion hops in three-dimensional covalently-bonded LATP and in $LiMXCl_4$. While LATP shows no correlated rotational motion for rotational events above 20°, $LiMXCl_4$ systems exhibit positive correlated rotational motion (positive ΔP values) for rotations between 20°-30°. This indicates that the van der Waals interactions in $LiMXCl_4$ enable a flexible framework that accommodates lithium-ion migration more effectively than the rigid covalent bonding in LATP.

The degree of correlation between hop and rotation events (ΔP) varies across different $LiMXCl_4$ chemistries and is directly related to the strength of interactions between Li ions and the nearby framework polyhedra (M-oct). A larger distance between the Li ions and non-Li cations or a larger free volume within the structure decreases these interactions, allowing Li ions to traverse relatively uncorrelated with polyhedral rotations These systems achieve high ionic conductivity

due to their wide and low-energy diffusion pathways. Similar observations have been made in amorphous Li_3PS_4 systems where lower density amorphous models tend to show smaller ΔP[41]. Therefore, the high ionic conductivity in $LiMXCl_4$ systems can be attributed to a favorable combination of several factors: a flat Li-ion energy landscape, low Li-ion density, a flexible and rotatable polyhedral framework, the soft-cradle effect, and weak repulsion between Li ions and other cations.

In the original article by Tanaka *et al*, the authors suggested a liquid-like diffusion behavior of lithium ions. This suggestion can be rationalized by the van der Waals framework of $LiMXCl_4$. Due to the weak van der Waals interactions in this framework, the M-octahedra frequently undergo orientational changes of substantial amplitude ($20°–30°$), resulting in a dynamic change of the lithium-ion site environment. This behavior contrasts sharply with other typical crystalline superionic conductors, such as garnet or NASICONs, where the framework remains mostly static leading to a non-changing diffusion network.

In this study, we performed a total of 42 ns of ab-initio molecular dynamics simulations across various chemistries, lithium contents, and temperatures. It has been reported that correlation factors require significantly longer simulations to achieve convergence compared to self-diffusion coefficients[30]. Consequently, we anticipate that the frequency of rotational events and the conditional probabilities relating different types of events may have larger uncertainties than the Li conductivity values computed assuming Nernst-Einstein relation. To address this, longer simulations in larger supercells that sample more rare events are desirable. We suggest that machine learning-based interatomic potentials[47–51] may provide an avenue towards more accurate

quantification of the correlations between Li-hops and octahedral tilting events.

4. Conclusion

In this work, we explore the effects of diverse chemical substitutions and Li-off stoichiometry in $LiMXCl_4$ systems. All the $LiMXCl_4$ chemistries we evaluated consistently exhibit superionic conductivity, and many of them are predicted to surpass the conductivity of previously explored materials like $LiTaOCl_4$ and $LiNbOCl_4$. The high ionic conductivities owing to their low activation energy and high conductivity prefactor, good deformability, and high voltage stability makes these systems highly promising for use as catholytes in all-solid-state batteries. Our probabilistic analysis of rotational dynamics on the picosecond timescale contributes direct, quantitative evidence of the soft tilting motion of MO_2Cl_4 octahedral groups that correlates with lithium-ion hops (ie. soft cradle effect) in $LiMXCl_4$, but this effect noticeably varies across different chemistries. We posit that the variation in correlated rotational motion across systems can be attributed to differences in free volume and octahedral volume. The flexibility of the van der Waals framework enables facile Li diffusion, even when there are increased Li-cation interactions or smaller free volumes, by flattening the Li energy landscape through 20-30° correlated octahedral rotations. Thus, the $LiMXCl_4$ framework is adaptable to changes in free volume and polyhedral size without compromising ionic conductivity. This adaptability is evident in the Meyer-Neldel analysis, which indicates that the $LiMXCl_4$ structures offer a favorable combination of low activation energy and high conductivity prefactor, making them promising for achieving even higher conductivity.

5. Methods

5.1 First principles calculations

All DFT calculations were performed using the Vienna Ab initio Simulation Package (VASP)[52] using the Perdew–Burke–Ernzerhof (PBE) generalized-gradient approximation (GGA)[53]. For AIMD simulations, the DFT-D3 (Grimme) van der Waals correction[54] was applied. An energy cutoff of 520 eV and a k-point density compatible with the Materials Project database[17] were used. A background charge was applied to maintain charge neutrality for the Li-deficient and Li-excess structures. For each system, three independent DFT relaxations were performed. Each relaxation was initiated from the cation- and anion- substituted $LVOF_4$ entry in the Materials Project (mp-850188). The results of the three relaxations are presented in Supporting Information, Table A-1. The first relaxation maintained the symmetry of the Tanaka et al. structure model (denoted as "symmetry on"). The two other relaxations were performed with the symmetry turned off (denoted as "symmetry off", ISYM = -1). One of the symmetry-off structures had the M-cation manually shifted upwards by 0.03 in fractional coordinates (denoted as "symmetry off, shifted"), while the other symmetry-off structure did not contain a manual shift (denoted as "symmetry off, no shift"). The lowest energy structure resulting from the three relaxations was used in the stability analysis. For the phase stability calculations, the vdW correction was not used to maintain compatibility with the Materials Project database. Structures with Li off-stoichiometry (Li-excess or Li-deficient) were created by adding or removing one Li ion to or from the relaxed symmetry-on stoichiometric structure and performing a DFT relaxation at constant volume with a compensating background charge. A Li vacancy was created by removing a randomly selected Li atom from the stoichiometric structure. For the Li-stuffed structure, symmetrically distinct Li ion sites were obtained by modeling the stoichiometric structure with the Buckingham potential[55]. A separate DFT calculation was

performed with a stuffed Li-ion for each candidate site and with a uniform background charge. The candidate site associated with the lowest DFT energy was selected as the site for the stuffed Li-ion.

5.2 Stability analysis

The thermodynamic stability of each LiMXCl$_4$ compound was determined by computing its energy above the convex hull of the relevant Li-M-X-Cl phase diagram. The electrochemical stability window for each LiMXCl$_4$ system was determined by constructing the grand potential $\Phi[c, \mu_{Li}]$ convex hull and varying μ_{Li} from 0 to 6V to identify the onset of decomposition at low and high μ_{Li}, following the procedure developed by Richards *et al*[24]. All compounds in the Materials Project database were considered as potential competing phases. Li$_2$ZrCl$_6$ and Li$_2$HfCl$_6$, which were experimentally reported but missing from the Materials Project database, were also included. In computing the stability window, we used the energy of the convex hull for metastable LiMXCl$_4$ systems to obtain a non-zero stability window. The energy of the lowest energy structure among the symmetry-on, symmetry-off without shift, and symmetry-off (detailed in Methods 5.1) structures was used for the computations.

5.3 Rotation and hop detection

For each MX$_2$Cl$_4$ octahedron, we recorded the rotation matrix required to reach the orientation at time *t* from the first snapshot using singular value decomposition, as implemented in a previous work[41]. We converted the rotation matrices to a unit quaternion and saved these quaternions throughout the entire trajectory. We then computed the quaternion distance between Q(t$_0$) and Q(t$_0$ + 1 ps) for t$_0$ values spanning the entire simulation. The quaternion distance between two

quaternions are computed by the equation: $d(q_1, q_2) = \min(2\log(q_1q_2^T), 2\log(-q_1q_2^T))$, which corresponds to the magnitude of the rotation angle needed to align q_1 to q_2. We detected peaks in the time series of quaternion distances with heights greater than the angle cutoff value and selected peaks with prominence larger than 50% of the angle cutoff values. Each detected peak indicates a rotation event occurred at time t_0, and the peak height corresponds to the angle of the rotation event. We chose the time interval of 1 ps because it is within the range of typical phonon frequencies. A similar algorithm was used to detect lithium-ion hops. We computed the distance between $R(t_0)$ (the position of lithium-ion at t_0) and $R(t_0 + 1\text{ ps})$ (the position of lithium-ion at $t_0 + 1$ ps) for t_0 values spanning the entire simulation, and detected peaks in the time series of distance values with heights greater than 3 Å. Our algorithm provides complete information on the initial orientation, final orientation, rotation angle, rotation axis, time of rotation event, and octahedra index for rotational events, as well as the initial position, final position, hop distance, time of hop event, and Li index for hop events. The error bars for the event frequencies of rotations and hops were computed based on the assumption that rotation or hop events are Poisson processes with no time correlation and a fixed rate constant.

5.4 Probability analysis of events

Based on the rotation and hop events detected in the MD trajectories, we compute the probability of rotational motion exceeding a specified angle under various conditions. To calculate P(rot | hop) (i.e. the probability of rotation assuming that the nearest neighboring lithium undergoes a hop within ± dt) for each lithium in the supercell, we first detected all hop events that occurred in the trajectory. We then identified allrotation events of its nearest neighboring MX_2Cl_4

octahedron within ± 2 ps of each hop event. We label the moment of each lithium hop as dt = 0 and identify the first rotation of the nearest neighboring octahedron following the hop (dt = t_{right} > 0) and the last rotation prior to the hop (dt = t_{left} < 0). For each lithium hop, we constructed a summed Heaviside step function $H(dt - t_{right}) + (1 - H(dt - t_{left}))$ to record the time taken for a rotation to follow or precede the hop event. By collecting such information for all lithium in the supercell, we averaged the summed Heaviside step functions to obtain the time-dependent conditional probability of rotation given that a hop event occurred at dt = 0.

A similar method was used to compute P(rot | no-hop) (i.e. the probability of rotation assuming that the nearest neighboring lithium did undergo a hop within ± dt timeframe) for each lithium in the supercell. For each lithium, we identified snapshots where the Li did not experience a hop within a ± 2 ps timeframe. For each of these snapshots, we constructed a Heaviside step function $H(dt-t_{right}) + (1-H(dt-t_{left}))$ to record the time taken for a rotation to follow or precede such a moment. By collecting this information for all snapshots where no hop occured within ± 2 ps, we computed the time-dependent conditional probability of rotation assuming no hop event occurred at dt = 0.

5.5 Ab-initio molecular dynamics

AIMD simulations of $LiMXCl_4$ systems were conducted with VASP at temperatures of 600, 650, 700, 750, and 800K. Simulations were performed on structure models that maintained the symmetry of Tanaka's structure model (symmetry on). The van der Waals correction was not used for the AIMD simulation of NASICON-type LATP. All MD calculations were carried out in the NVT ensemble using a Nóse-Hoover thermostat, with volumes fixed at the values of the 0 K relaxed structures. For each temperature and system, the temperature was linearly ramped from 100 K to the target temperature by scaling the velocities at intervals of 0.2 ps for 2 ps. Following this, an equilibration period of 5 ps was performed at the target temperature, followed by a long simulation at the desired temperature for at least 400 ps. The timestep of 2 fs was used. Li-ion self-diffusion coefficients were determined by calculating the mean squared displacements (MSD) of the AIMD annealing trajectories, where the squared displacements were averaged over time intervals of duration Δt. Only the portion of the MSD curve with $\Delta t > 1$ ps and $\Delta t < 10\%$ of the total simulation time was considered in the analysis. Error bars for the diffusivities were computed using the empirical error estimation scheme proposed by He et al[56]. Activation energies and room temperature diffusivities were extrapolated by fitting the diffusivities to an Arrhenius relation. Ionic conductivities were calculated from Li-ion self-diffusivities assuming the Nernst-Einstein relation.

5.6 Meyer-Neldel relationship

The Meyer-Neldel rule (MNR) specifies a linear relationship between $\ln\sigma_0$ and E_a in the form $\ln\sigma_0 = \alpha E_a + \beta$, and $\Delta_0 = 1/\alpha$ is the Meyer-Neldel energy[57]. The conductivity prefactor σ_0 is determined from the Arrhenius relation used to fit the simulation diffusivities, as described in

Section 5.5. The coefficients α and β are obtained by performing linear regression of $\ln\sigma_0$ vs. E_a data for all $LiMXCl_4$ systems except $LiSbOCl_4$. The guidelines in Fig. 4c are derived by taking the logarithm of the Arrhenius conductivity relation $\sigma T = \sigma_0 e^{(\frac{E_a}{k_B T})}$ and rearranging it, which leads to $\ln\sigma_0 = \ln\sigma T + \frac{E_a}{k_B T}$. This indicates a linear relationship between E_a and $\ln\sigma_0$ with a slope of $\frac{1}{k_B T}$ and an intercept of $\ln(\sigma T)$. Thus, by inputting the desired temperature (300K in our case) and conductivity (10^{-3} to 10^3 mS/cm), we obtain the guidelines shown in Fig. 4c.

views and opinions of authors expressed herein do not necessarily state or reflect those of the

United States Government or any agency thereof.

Conflicts of interest

The authors declare no conflict of interest.

References

(1) Zhao, Q.; Stalin, S.; Zhao, C.-Z.; Archer, L. A. Designing Solid-State Electrolytes for Safe, Energy-Dense Batteries. *Nat. Rev. Mater.* **2020**, *5* (3), 229–252. https://doi.org/10.1038/s41578-019-0165-5.

(2) Xiao, Y.; Wang, Y.; Bo, S.-H.; Kim, J. C.; Miara, L. J.; Ceder, G. Understanding Interface Stability in Solid-State Batteries. *Nat. Rev. Mater.* **2020**, *5* (2), 105–126. https://doi.org/10.1038/s41578-019-0157-5.

(3) Zhou, L.; Zuo, T.-T.; Kwok, C. Y.; Kim, S. Y.; Assoud, A.; Zhang, Q.; Janek, J.; Nazar, L. F. High Areal Capacity, Long Cycle Life 4 V Ceramic All-Solid-State Li-Ion Batteries Enabled by Chloride Solid Electrolytes. *Nat. Energy* **2022**, *7* (1), 83–93. https://doi.org/10.1038/s41560-021-00952-0.

(4) Hayashi, N.; Watanabe, K.; Shimanoe, K. Co-Sintering a Cathode Material and Garnet Electrolyte to Develop a Bulk-Type Solid-State Li Metal Battery with Wide Electrochemical Windows. *J. Mater. Chem. A* **2024**, *12* (9), 5269–5281. https://doi.org/10.1039/D3TA06747E.

(5) Demuth, T.; Fuchs, T.; Walther, F.; Pokle, A.; Ahmed, S.; Malaki, M.; Beyer, A.; Janek, J.; Volz, K. Influence of the Sintering Temperature on LLZO-NCM Cathode Composites for Solid-State Batteries Studied by Transmission Electron Microscopy. *Matter* **2023**, *6* (7), 2324–2339. https://doi.org/10.1016/j.matt.2023.04.022.

(6) Kwak, H.; Wang, S.; Park, J.; Liu, Y.; Kim, K. T.; Choi, Y.; Mo, Y.; Jung, Y. S. Emerging Halide Superionic Conductors for All-Solid-State Batteries: Design, Synthesis, and Practical Applications. *ACS Energy Lett.* **2022**, *7* (5), 1776–1805. https://doi.org/10.1021/acsenergylett.2c00438.

(7) Wang, C.; Liang, J.; Kim, J. T.; Sun, X. Prospects of Halide-Based All-Solid-State Batteries: From Material Design to Practical Application. *Sci. Adv.* **2022**, *8* (36), eadc9516. https://doi.org/10.1126/sciadv.adc9516.

(8) Liang, J.; Li, X.; Adair, K. R.; Sun, X. Metal Halide Superionic Conductors for All-Solid-State Batteries. *Acc. Chem. Res.* **2021**, *54* (4), 1023–1033. https://doi.org/10.1021/acs.accounts.0c00762.

(9) Asano, T.; Sakai, A.; Ouchi, S.; Sakaida, M.; Miyazaki, A.; Hasegawa, S. Solid Halide Electrolytes with High Lithium-Ion Conductivity for Application in 4 V Class Bulk-Type All-Solid-State Batteries. *Adv. Mater.* **2018**, *30* (44), 1803075. https://doi.org/10.1002/adma.201803075.

(10) Kamaya, N.; Homma, K.; Yamakawa, Y.; Hirayama, M.; Kanno, R.; Yonemura, M.; Kamiyama, T.; Kato, Y.; Hama, S.; Kawamoto, K.; Mitsui, A. A Lithium Superionic Conductor. *Nat. Mater.* **2011**, *10* (9), 682–686. https://doi.org/10.1038/nmat3066.

(11) Zhou, L.; Assoud, A.; Zhang, Q.; Wu, X.; Nazar, L. F. New Family of Argyrodite Thioantimonate Lithium Superionic Conductors. *J. Am. Chem. Soc.* **2019**, *141* (48), 19002–19013. https://doi.org/10.1021/jacs.9b08357.

(12) Li, Y.; Song, S.; Kim, H.; Nomoto, K.; Kim, H.; Sun, X.; Hori, S.; Suzuki, K.; Matsui, N.; Hirayama, M.; Mizoguchi, T.; Saito, T.; Kamiyama, T.; Kanno, R. A Lithium Superionic Conductor for Millimeter-Thick Battery Electrode. *Science* **2023**, *381* (6653), 50–53. https://doi.org/10.1126/science.add7138.

(13) Luo, J.-D.; Zhang, Y.; Cheng, X.; Li, F.; Tan, H.-Y.; Zhou, M.-Y.; Wang, Z.-W.; Hao, X.-D.; Yin, Y.-C.; Jiang, B.; Yao, H.-B. Halide Superionic Conductors with Non-Close-Packed Anion Frameworks. *Angew. Chem. Int. Ed.* **2024**, *63* (17), e202400424. https://doi.org/10.1002/anie.202400424.

(14) Tanaka, Y.; Ueno, K.; Mizuno, K.; Takeuchi, K.; Asano, T.; Sakai, A. New Oxyhalide Solid Electrolytes with High Lithium Ionic Conductivity >10 mS Cm−1 for All-Solid-State Batteries. *Angew. Chem.* **2023**, *135* (13), e202217581.

https://doi.org/10.1002/ange.202217581.

(15) Singh, B.; Wang, Y.; Liu, J.; Bazak, J. D.; Shyamsunder, A.; Nazar, L. F. Critical Role of Framework Flexibility and Disorder in Driving High Ionic Conductivity in LiNbOCl4. *J. Am. Chem. Soc.* **2024**. https://doi.org/10.1021/jacs.4c03142.

(16) Hautier, G.; Fischer, C.; Ehrlacher, V.; Jain, A.; Ceder, G. Data Mined Ionic Substitutions for the Discovery of New Compounds. *Inorg. Chem.* **2011**, *50* (2), 656–663. https://doi.org/10.1021/ic102031h.

(17) Jain, A.; Ong, S. P.; Hautier, G.; Chen, W.; Richards, W. D.; Dacek, S.; Cholia, S.; Gunter, D.; Skinner, D.; Ceder, G.; Persson, K. A. Commentary: The Materials Project: A Materials Genome Approach to Accelerating Materials Innovation. *APL Mater.* **2013**, *1* (1), 011002. https://doi.org/10.1063/1.4812323.

(18) Adams, S. Origin of Fast Li+-Ion Conductivity in the Compressible Oxyhalide LiNbOCl4. *Energy Storage Mater.* **2024**, *68*, 103359. https://doi.org/10.1016/j.ensm.2024.103359.

(19) Kunz, M.; Brown, I. D. Out-of-Center Distortions around Octahedrally Coordinated *d*0 Transition Metals. *J. Solid State Chem.* **1995**, *115* (2), 395–406. https://doi.org/10.1006/jssc.1995.1150.

(20) Halasyamani, P. S. Asymmetric Cation Coordination in Oxide Materials: Influence of Lone-Pair Cations on the Intra-Octahedral Distortion in D0 Transition Metals. *Chem. Mater.* **2004**, *16* (19), 3586–3592. https://doi.org/10.1021/cm049297g.

(21) Wang, S.; Bai, Q.; Nolan, A. M.; Liu, Y.; Gong, S.; Sun, Q.; Mo, Y. Lithium Chlorides and Bromides as Promising Solid-State Chemistries for Fast Ion Conductors with Good Electrochemical Stability. *Angew. Chem. Int. Ed.* **2019**, *58* (24), 8039–8043. https://doi.org/10.1002/anie.201901938.

(22) Aykol, M.; Dwaraknath, S. S.; Sun, W.; Persson, K. A. Thermodynamic Limit for Synthesis of Metastable Inorganic Materials. *Sci. Adv.* **2018**, *4* (4), eaaq0148. https://doi.org/10.1126/sciadv.aaq0148.

(23) Sun, W.; Dacek, S. T.; Ong, S. P.; Hautier, G.; Jain, A.; Richards, W. D.; Gamst, A. C.; Persson, K. A.; Ceder, G. The Thermodynamic Scale of Inorganic Crystalline Metastability. *Sci. Adv.* **2016**, *2* (11), e1600225. https://doi.org/10.1126/sciadv.1600225.

(24) Richards, W. D.; Miara, L. J.; Wang, Y.; Kim, J. C.; Ceder, G. Interface Stability in Solid-State Batteries. *Chem. Mater.* **2016**, *28* (1), 266–273. https://doi.org/10.1021/acs.chemmater.5b04082.

(25) Zhu, Y.; He, X.; Mo, Y. Origin of Outstanding Stability in the Lithium Solid Electrolyte Materials: Insights from Thermodynamic Analyses Based on First-Principles Calculations. *ACS Appl. Mater. Interfaces* **2015**, *7* (42), 23685–23693. https://doi.org/10.1021/acsami.5b07517.

(26) Xiao, Y.; Miara, L. J.; Wang, Y.; Ceder, G. Computational Screening of Cathode Coatings for Solid-State Batteries. *Joule* **2019**, *3* (5), 1252–1275. https://doi.org/10.1016/j.joule.2019.02.006.

(27) Seo, D.-H.; Lee, J.; Urban, A.; Malik, R.; Kang, S.; Ceder, G. The Structural and Chemical Origin of the Oxygen Redox Activity in Layered and Cation-Disordered Li-Excess Cathode Materials. *Nat. Chem.* **2016**, *8* (7), 692–697. https://doi.org/10.1038/nchem.2524.

(28) Xiao, Y.; Jun, K.; Wang, Y.; Miara, L. J.; Tu, Q.; Ceder, G. Lithium Oxide Superionic Conductors Inspired by Garnet and NASICON Structures. *Adv. Energy Mater.* **2021**, *11* (37), 2101437. https://doi.org/10.1002/aenm.202101437.

(29) Jun, K.; Sun, Y.; Xiao, Y.; Zeng, Y.; Kim, R.; Kim, H.; Miara, L. J.; Im, D.; Wang, Y.; Ceder, G. Lithium Superionic Conductors with Corner-Sharing Frameworks. *Nat. Mater.* **2022**, *21* (8), 924–931. https://doi.org/10.1038/s41563-022-01222-4.

(30) Marcolongo, A.; Marzari, N. Ionic Correlations and Failure of Nernst-Einstein Relation in Solid-State Electrolytes. *Phys. Rev. Mater.* **2017**, *1* (2), 025402. https://doi.org/10.1103/PhysRevMaterials.1.025402.

(31) Zhong, P.; Gupta, S.; Deng, B.; Jun, K.; Ceder, G. Effect of Cation Disorder on Lithium Transport in Halide Superionic Conductors. *ACS Energy Lett.* **2024**, 2775–2781. https://doi.org/10.1021/acsenergylett.4c00799.

(32) Liu, Y.; Wang, S.; Nolan, A. M.; Ling, C.; Mo, Y. Tailoring the Cation Lattice for Chloride Lithium-Ion Conductors. *Adv. Energy Mater.* **2020**, *10* (40), 2002356. https://doi.org/10.1002/aenm.202002356.

(33) Yin, Y.-C.; Yang, J.-T.; Luo, J.-D.; Lu, G.-X.; Huang, Z.; Wang, J.-P.; Li, P.; Li, F.; Wu, Y.-C.; Tian, T.; Meng, Y.-F.; Mo, H.-S.; Song, Y.-H.; Yang, J.-N.; Feng, L.-Z.; Ma, T.; Wen, W.; Gong, K.; Wang, L.-J.; Ju, H.-X.; Xiao, Y.; Li, Z.; Tao, X.; Yao, H.-B. A LaCl3-Based Lithium Superionic Conductor Compatible with Lithium Metal. *Nature* **2023**, *616* (7955), 77–83. https://doi.org/10.1038/s41586-023-05899-8.

(34) Gao, Y.; Li, N.; Wu, Y.; Yang, W.; Bo, S.-H. Rethinking the Design of Ionic Conductors Using Meyer–Neldel–Conductivity Plot. *Adv. Energy Mater.* **2021**, *11* (13), 2100325. https://doi.org/10.1002/aenm.202100325.

(35) Muy, S.; Bachman, J. C.; Chang, H.-H.; Giordano, L.; Maglia, F.; Lupart, S.; Lamp, P.; Zeier, W. G.; Shao-Horn, Y. Lithium Conductivity and Meyer-Neldel Rule in Li3PO4–Li3VO4–Li4GeO4 Lithium Superionic Conductors. *Chem. Mater.* **2018**, *30* (16), 5573–5582. https://doi.org/10.1021/acs.chemmater.8b01504.

(36) Flores-González, N.; López, M.; Minafra, N.; Bohnenberger, J.; Viñes, F.; Rudić, S.; Krossing, I.; G. Zeier, W.; Illas, F.; H. Gregory, D. Understanding the Effect of Lattice Polarisability on the Electrochemical Properties of Lithium Tetrahaloaluminates, LiAlX 4 (X = Cl, Br, I). *J. Mater. Chem. A* **2022**, *10* (25), 13467–13475. https://doi.org/10.1039/D2TA02821B.

(37) Krauskopf, T.; Pompe, C.; Kraft, M. A.; Zeier, W. G. Influence of Lattice Dynamics on Na+ Transport in the Solid Electrolyte Na3PS4–xSex. *Chem. Mater.* **2017**, *29* (20), 8859–8869. https://doi.org/10.1021/acs.chemmater.7b03474.

(38) Kraft, M. A.; Culver, S. P.; Calderon, M.; Böcher, F.; Krauskopf, T.; Senyshyn, A.; Dietrich, C.; Zevalkink, A.; Janek, J.; Zeier, W. G. Influence of Lattice Polarizability on the Ionic Conductivity in the Lithium Superionic Argyrodites Li6PS5X (X = Cl, Br, I). *J. Am. Chem. Soc.* **2017**, *139* (31), 10909–10918. https://doi.org/10.1021/jacs.7b06327.

(39) Murugan, R.; Thangadurai, V.; Weppner, W. Fast Lithium Ion Conduction in Garnet-Type Li(7)La(3)Zr(2)O(12). *Angew. Chem. Int. Ed Engl.* **2007**, *46* (41), 7778–7781. https://doi.org/10.1002/anie.200701144.

(40) Li, X.; Liang, J.; Adair, K. R.; Li, J.; Li, W.; Zhao, F.; Hu, Y.; Sham, T.-K.; Zhang, L.; Zhao, S.; Lu, S.; Huang, H.; Li, R.; Chen, N.; Sun, X. Origin of Superionic Li3Y1–xInxCl6 Halide Solid Electrolytes with High Humidity Tolerance. *Nano Lett.* **2020**, *20* (6), 4384–4392. https://doi.org/10.1021/acs.nanolett.0c01156.

(41) Jun, K.; Lee, B.; L. Kam, R.; Ceder, G. The Nonexistence of a Paddlewheel Effect in Superionic Conductors. *Proc. Natl. Acad. Sci.* **2024**, *121* (18), e2316493121. https://doi.org/10.1073/pnas.2316493121.

(42) Huynh, D. Q. Metrics for 3D Rotations: Comparison and Analysis. *J. Math. Imaging Vis.* **2009**, *35* (2), 155–164. https://doi.org/10.1007/s10851-009-0161-2.

(43) Sebti, E.; Evans, H. A.; Chen, H.; Richardson, P. M.; White, K. M.; Giovine, R.; Koirala, K. P.; Xu, Y.; Gonzalez-Correa, E.; Wang, C.; Brown, C. M.; Cheetham, A. K.; Canepa, P.; Clément, R. J. Stacking Faults Assist Lithium-Ion Conduction in a Halide-Based Superionic Conductor. *J. Am. Chem. Soc.* **2022**, *144* (13), 5795–5811. https://doi.org/10.1021/jacs.1c11335.

(44) Xu, M.; Park, M. S.; Lee, J. M.; Kim, T. Y.; Park, Y. S.; Ma, E. Mechanisms of Li^{+} Transport in Garnet-Type Cubic $Li_{3+x}La_{3}M_{2}O_{12}$ (M = Te, Nb, Zr). *Phys. Rev. B* **2012**, *85* (5), 052301. https://doi.org/10.1103/PhysRevB.85.052301.

(45) Aono, H.; Sugimoto, E.; Sadaoka, Y.; Imanaka, N.; Adachi, G. Ionic Conductivity of Solid Electrolytes Based on Lithium Titanium Phosphate. *J. Electrochem. Soc.* **1990**, *137* (4), 1023. https://doi.org/10.1149/1.2086597.

(46) Aono, H.; Sugimoto, E.; Sadaoka, Y.; Imanaka, N.; Adachi, G. Ionic Conductivity and Sinterability of Lithium Titanium Phosphate System. *Solid State Ion.* **1990**, *40–41*, 38–42. https://doi.org/10.1016/0167-2738(90)90282-V.

(47) Deng, B.; Zhong, P.; Jun, K.; Riebesell, J.; Han, K.; Bartel, C. J.; Ceder, G. CHGNet as a Pretrained Universal Neural Network Potential for Charge-Informed Atomistic Modelling. *Nat. Mach. Intell.* **2023**, *5* (9), 1031–1041. https://doi.org/10.1038/s42256-023-00716-3.

(48) Musaelian, A.; Batzner, S.; Johansson, A.; Sun, L.; Owen, C. J.; Kornbluth, M.; Kozinsky, B. Learning Local Equivariant Representations for Large-Scale Atomistic Dynamics. *Nat. Commun.* **2023**, *14* (1), 579. https://doi.org/10.1038/s41467-023-36329-y.

(49) Chen, C.; Ong, S. P. A Universal Graph Deep Learning Interatomic Potential for the Periodic Table. *Nat. Comput. Sci.* **2022**, *2* (11), 718–728. https://doi.org/10.1038/s43588-022-00349-3.

(50) Batzner, S.; Musaelian, A.; Sun, L.; Geiger, M.; Mailoa, J. P.; Kornbluth, M.; Molinari, N.; Smidt, T. E.; Kozinsky, B. E(3)-Equivariant Graph Neural Networks for Data-Efficient and Accurate Interatomic Potentials. *Nat. Commun.* **2022**, *13* (1), 2453. https://doi.org/10.1038/s41467-022-29939-5.

(51) Batatia, I.; Benner, P.; Chiang, Y.; Elena, A. M.; Kovács, D. P.; Riebesell, J.; Advincula, X. R.; Asta, M.; Avaylon, M.; Baldwin, W. J.; Berger, F.; Bernstein, N.; Bhowmik, A.; Blau, S. M.; Cărare, V.; Darby, J. P.; De, S.; Della Pia, F.; Deringer, V. L.; Elijošius, R.; El-Machachi, Z.; Falcioni, F.; Fako, E.; Ferrari, A. C.; Genreith-Schriever, A.; George, J.; Goodall, R. E. A.; Grey, C. P.; Grigorev, P.; Han, S.; Handley, W.; Heenen, H. H.; Hermansson, K.; Holm, C.; Jaafar, J.; Hofmann, S.; Jakob, K. S.; Jung, H.; Kapil, V.; Kaplan, A. D.; Karimitari, N.; Kermode, J. R.; Kroupa, N.; Kullgren, J.; Kuner, M. C.; Kuryla, D.; Liepuoniute, G.; Margraf, J. T.; Magdău, I.-B.; Michaelides, A.; Moore, J. H.; Naik, A. A.; Niblett, S. P.; Norwood, S. W.; O'Neill, N.; Ortner, C.; Persson, K. A.; Reuter, K.; Rosen, A. S.; Schaaf, L. L.; Schran, C.; Shi, B. X.; Sivonxay, E.; Stenczel, T. K.; Svahn, V.; Sutton, C.; Swinburne, T. D.; Tilly, J.; van der Oord, C.; Varga-Umbrich, E.; Vegge, T.; Vondrák, M.; Wang, Y.; Witt, W. C.; Zills, F.; Csányi, G. *A foundation model for atomistic materials chemistry*. arXiv.org. https://arxiv.org/abs/2401.00096v2 (accessed 2024-06-22).

(52) Kresse, G.; Furthmüller, J. Efficient Iterative Schemes for Ab Initio Total-Energy Calculations Using a Plane-Wave Basis Set. *Phys. Rev. B* **1996**, *54* (16), 11169–11186. https://doi.org/10.1103/PhysRevB.54.11169.

(53) Perdew, J. P.; Burke, K.; Ernzerhof, M. Generalized Gradient Approximation Made Simple. *Phys. Rev. Lett.* **1996**, *77* (18), 3865–3868. https://doi.org/10.1103/PhysRevLett.77.3865.

(54) Grimme, S.; Antony, J.; Ehrlich, S.; Krieg, H. A Consistent and Accurate Ab Initio Parametrization of Density Functional Dispersion Correction (DFT-D) for the 94 Elements H-Pu. *J. Chem. Phys.* **2010**, *132* (15), 154104. https://doi.org/10.1063/1.3382344.

(55) Ogorodnikov, V. V.; Rogovoi, Yu. I. Buckingham-Potential Parameters and Relations between Them for Solids. *Powder Metall. Met. Ceram.* **1995**, *33* (5), 327–333. https://doi.org/10.1007/BF00560208.

(56) He, X.; Zhu, Y.; Epstein, A.; Mo, Y. Statistical Variances of Diffusional Properties from Ab Initio Molecular Dynamics Simulations. *Npj Comput. Mater.* **2018**, *4* (1), 1–9. https://doi.org/10.1038/s41524-018-0074-y.

(57) Meyer, W.; Neldel, H. *Z Techn Phys* **1937**, *12* (588).